Beam Performance

Developments and Upgrades of Storage Ring

Improvement of Dynamic Aperture by Counter-Sextupole Magnets

In the SPring-8 storage ring, there are four magnet-free long straight sections of 30 m length. These long straight sections were installed in 2000 by locally rearranging quadrupole and sextupole magnets. At that time, we maintained the periodicity of the cell structure, particularly that of sextupole field distribution along the ring, since the high periodicity leads to the large dynamic aperture. To maintain the periodicity as high as possible, we adopted a scheme in which "betatron phase matching" and "local chromaticity correction" are combined. The betatron phase matching keeps the dynamic aperture for on-momentum particles large and the latter enlarges that for off-momentum ones with local chromaticity correction by focusing sextupole magnets (SFL) in matching cells. However, the nonlinear kick of the SFL slightly breaks the periodicity and reduces the dynamic aperture.

To improve the symmetry of the storage ring, we installed "counter-sextupole magnets" (SCT) in every long straight section in 2007 [1-3]. These magnets are placed π apart from the SFL in the horizontal betatron phase, so they can minimize the harmful nonlinear kick of the SFL. After installing the SCT, we confirmed the enlargement of the dynamic aperture by measuring the injection efficiency. Figure 1 shows the dependence of the injection efficiency on the gaps of the in-vacuum undulators, ID20 and ID23. From the measurement, we found that the injection efficiency is improved by 6% by the SCT, which contributes to the stable top-up operation.

Recently, to investigate the nonlinear dynamics of the storage ring, especially the effect of the SCT, we directly measured the dynamical aperture. Observing the survival rate of the stored beam after instantly giving the horizontal displacement by the pulse bump magnets, we measured the horizontal dynamical aperture. The survival rate is given by the ratio of the stored currents before and after the kick caused by the bump magnets, or that of the voltage sums of 4 electrodes of the turn-by-turn beam position monitors. The latter can give the decay process of the survival rate as well as the oscillation of the beam, so it is suitable to analyze the nonlinear dynamics.

Figure 2 shows the dependence of the survival rates obtained by turning the SCT on and off, from which we can estimate the dynamic aperture. Note that the reduction of the survival rate at both the ends in the case of the SCT on is limited not by the dynamical but the physical apertures. This is found from the decay process of the survival rate. In the case of the SCT on, the survival rates at the ends suddenly drop at the first turn, which means that the stored electrons are lost because of the physical aperture. Thus, the dynamic aperture with the SCT is larger than that as observed in Fig. 2. The measured dynamic aperture in the case of turning the SCT off is estimated to be the horizontal displacements at which the survival rate decreases. We find that the estimated dynamic aperture fairly well agrees with that estimated by computer simulation.

To investigate the mechanism of limiting the dynamic aperture, we analyzed the beam oscillation after the sudden displacement. The Fourier analysis of the oscillation gives the dependence of the betatron tune on the displacement, i.e., the amplitude, as shown in Fig. 3. The circles and crosses in the figure represent the horizontal and vertical betatron tunes,

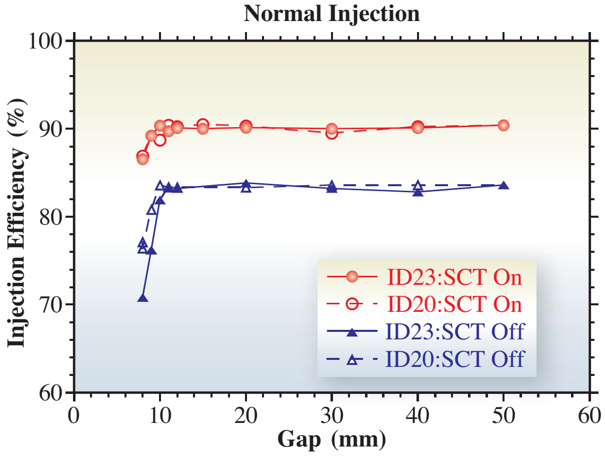

Fig. 1. Injection efficiency *vs*. in-vacuum undulator gaps.

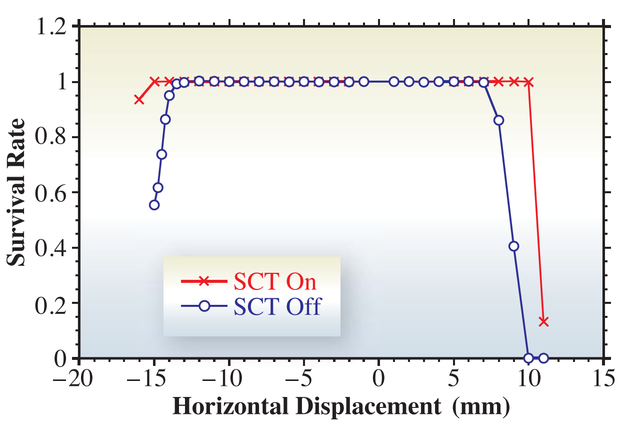

Fig. 2. Dependence of the survival rate on the displacement caused by the bump magnet.

respectively, and the dotted lines denote the calculated ones. As expected, we find from Fig. 3 that the amplitude-dependent tune shift is reduced by the SCT, and namely, that the nonlinear kick is weakened. Plotting the horizontal and vertical tunes on a map, we obtain the tune diagram shown in Fig. 4. The axes indicate the fractional parts of the betatron tunes, and the dashed lines represent the nearest third-order resonances, and the dotted lines represent the higher ones. Then we can conclude that, in the case of the SCT off, the dynamic aperture is limited by the normal sextupole resonance $\nu_x+2\nu_y=77$.

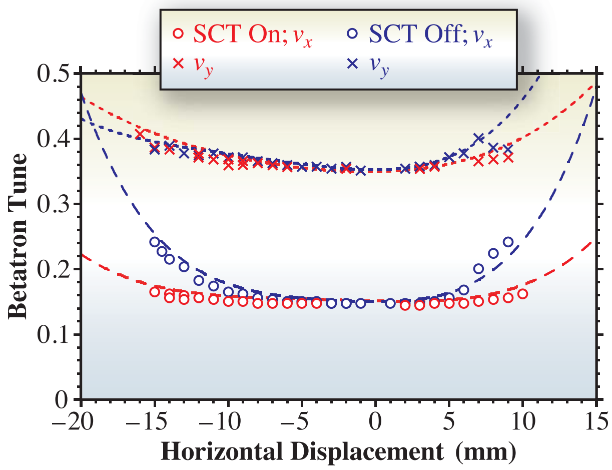

Fig. 3. Amplitude-dependent tune shift.

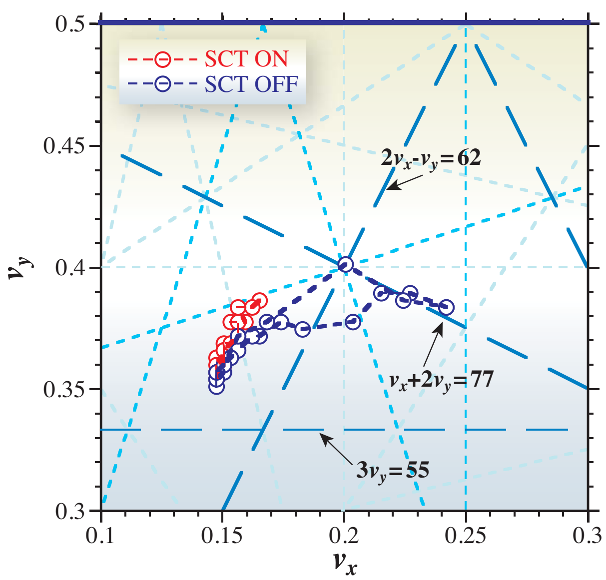

Fig. 4. Tune diagram.

Short-Bunch Operation with Low-α Optics

The length of circulating electron bunches can be made shorter by changing the storage ring optics to that having a smaller value of momentum compaction factor α. For the nominal optics in user time the lowest order term (see below) is $\alpha_0=1.68\times10^{-4}$ and the rms bunch length σ is 13 ps at the limit of zero bunch current. Since the bunch length σ is proportional to the square root of α at low bunch current, we can reduce σ by adopting low-α optics for generating shorter X-ray pulses.

The momentum compaction factor α represents the dependence of path length on momentum deviation $\Delta p/p$ of an electron and can be written as $\alpha=\alpha_0+\alpha_1(\Delta p/p)+\alpha_2(\Delta p/p)^2+\ldots$. Although the lowest order term α_0 is dominant in conventional optics, its value can be lowered by changing quadrupole strengths in the arc section in exchange for increasing the emittance. Figure 5 is an example of such low-α optics, where optical functions are shown for a quarter of the storage ring. We see that the horizontal dispersion function η_x is positive at arc sections and negative at straight sections, and this enables us to reduce α. For the optics shown in Fig. 5, the reduction factor in α_0 is 11 although the emittance increases by a factor of 7. The value of α_0 can be reduced further by carefully tuning quadrupole strengths. In such optics with an extremely small α_0, however, the next order term $\alpha_1(\Delta p/p)$ is dominant and the energy oscillation of electrons within a bunch becomes unstable. We then need to reduce α_1 at the same time and this can be carried out by tuning sextupole strengths in the arc section.

We optimized quadrupole and sextupole strengths and carried out beam tests with low-α

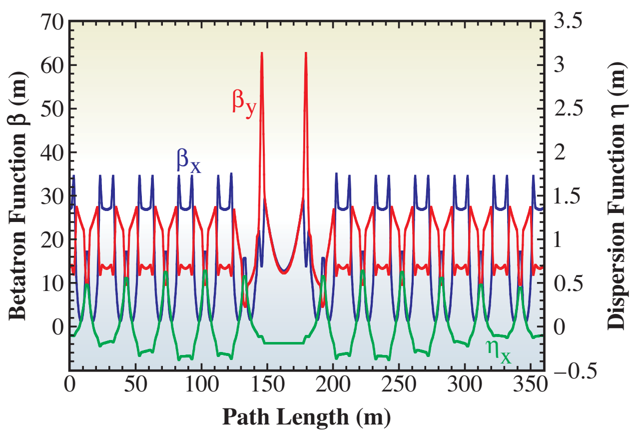

Fig. 5. Low-α optics. The horizontal and vertical betatron functions (β_x and β_y) and dispersion function (η_x) are shown for a quarter of the ring.

optics. By reducing α_0 and α_1 and measuring the bunch length σ with an optical streak camera at a low bunch current of 0.01 mA, we obtained the α_0-dependence of σ as shown in Fig. 6. The shortest bunch length of 2.2 ps was achieved for the optics with $\alpha_0=5.8\times10^{-6}$. This optics with σ=2.2 ps, however, has a very short beam lifetime due to a narrow range of energy acceptance. For stable beam operation of this optics, we further need to carefully tune the sextupoles. In addition, we also found by computer simulations that octupole magnets are effective in controlling α_2 and enlarging the energy acceptance. Further studies on these are necessary for the stable operation of the low-α optics.

To observe the performance of the low-α optics, we carried out a test experiment in the 25-m-long undulator beamline. A total current of 0.14 mA was stored in 12 bunches. The optics used has $\alpha_0=1.61\times10^{-5}$ and the bunch length was measured to be σ=4 ps. The data analysis is in progress.

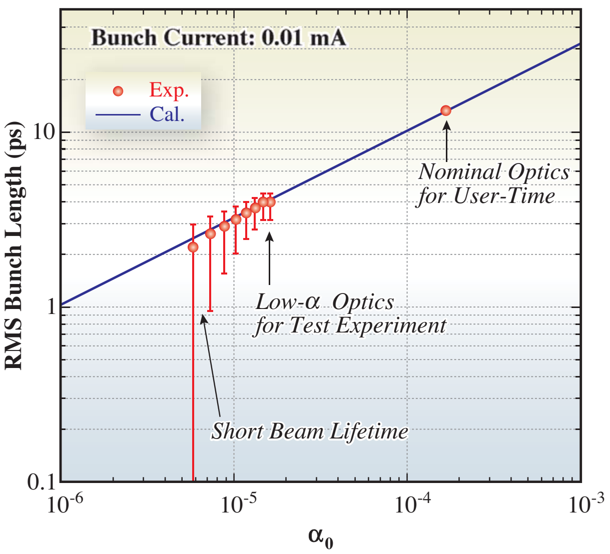

Fig. 6. RMS bunch length at a low bunch current of 0.01 mA as a function of α_0. The experimental data was obtained using an optical streak camera whose time-scale had been calibrated with a stored beam. The timing jitter was estimated to be 2.5 ± 1 ps and corresponding error bars are shown.

Suppression of the Filling Pattern Dependence of the BPM Signal Processing Electronics

The signal processing electronics of the storage ring beam position monitors (BPMs) were replaced during the summer shutdown of 2006 and it was found that they had the filling pattern dependence as large as over a hundred micrometers, as reported in Research Frontiers 2007. In addition, it was reported in Research Frontiers 2007 that the countermeasure to suppress the filling pattern dependence was to attach the band pass filters (BPFs) at the input of each channel of the electronics, and preliminary results showed the effectiveness of the BPF. In 2008, the production version BPF was made, attached to all the electrode channels, and the performance was evaluated using the actual beam.

The BPFs were attached during the short shutdown period from the end of October to the beginning of November. After the storage ring operation was restarted, no significant indication concerning the filling pattern dependence was reported for ordinary user operations.

During the machine study period, the effect of BPF was evaluated. As a measure of the effect, root mean square (RMS) values between two different measurements of the closed orbit distortion (COD), averaged over all the BPM, were used, which were defined as

$$RMS_x\,(A\text{-}B)=\sqrt{\frac{\sum_{i=1}^{N_{BPM}}\left(x_i^A-x_i^B\right)^2}{N_{BPM}}}\ ,\quad RMS_y\,(A\text{-}B)=\sqrt{\frac{\sum_{i=1}^{N_{BPM}}\left(y_i^A-y_i^B\right)^2}{N_{BPM}}}$$

where RMS_x is in the horizontal direction and RMS_y is in the vertical direction, the superscripts A and B indicates the two different measurements: measurement A and measurement B, i runs through 1 to the number of BPM N_{BPM}, x_i and y_i are the measured position values in the horizontal and vertical directions of i-th BPM.

The filling patterns in Table 1 were selected for the evaluation. These filling patterns were taken from the typical user runs. The storage ring was operated with 100 mA total stored current for all the patterns in Table 1. The change in the measured values of the COD between two different patterns was estimated using the RMS values between the COD measurements of the two different filling patterns, which were expressed as $RMS_{x/y}$*(FP1-FP2)* according the equation, where *FP1* and *FP2* are the indices of the filling patterns.

During the evaluation runs, the periodic COD correction was switched off. The COD correction was carried out during ordinary user runs to compensate the drift of the beam orbit itself. However, the correction process induced an artificial jump of COD by exciting the steering magnets that introduced some difficulties in evaluating the filling pattern dependence of the electronics.

The stored beam had to be discarded and refilled for the filling pattern to be changed, and it took approximately or over 20 minutes. During the time of the filling pattern change, the COD continued to drift. The RMS values between two different filling patterns, $RMS_{x/y}(FP1\text{-}FP2)$, should be compared with the RMS values caused by the orbit drift in the same amount of time for the filling pattern change. For comparison, we used the same procedure except for changing the filling pattern: the beam was discarded and refilled without changing the filling patterns and calculated RMS values, $RMS_{x/y}(FP1_1\text{-}FP1_2)$, where $FP1_1$ and $FP1_2$ are the indices of the two different measurements of the same filling pattern *FP1*.

Table 1 shows the RMS values of the differences between the COD measurements just before the discard and just after the refill of the beam with a different filling pattern. Table 2 is for the RMS values of the differences between the COD measurements just before the discard and just after the refill of the beam without changing the filling pattern. The time intervals of the two measurements in both Tables 1 and 2 were about the same, and the RMS values in both tables showed no significant difference. The main effect on the RMS values in both Tables 1 and 2 was the drift of the closed orbit during the interval of two measurements. Therefore, no significant differences in the measured beam position attributed to the filling pattern dependence of the electronics were observed.

In Fig. 7, the RMS evolution from the beginning of the measurement for the evaluation, $RMS_{x/y}(t\text{-}t_0)$, is shown. The RMS values were obtained for the differences in the position data from the reference COD measurement that was carried out at the beginning, t_0, of the evaluation runs. The filling patterns were changed in the order that is indicated in the figure: multi-bunches, 203 bunches, 1/12+10 s, and 1/14+12 s. Each filling pattern was repeated twice to estimate the reproducibility.

The RMS tended to increase almost monotonically in both *x* and *y* directions, regardless of the change in the filling pattern. No significant jump of the data between the different filling patterns was observed in the plot. The drift of the closed orbit was the dominant effect of the evolution of the RMS values.

Thus, the closed orbits can be set continuously across any filling pattern for the ordinary user run of the storage ring.

Table 1. RMS values of differences between two different filling patterns: $RMS_{x/y}(FP1\text{-}FP2)$

filling pattern 1	filling pattern 2	Δt (min. : sec.)	RMS_x (mm)	RMS_y (mm)
multi-bunches	203 bunches	24:20	6.8	2.9
203 bunches	1/12+10s	19:48	4.2	4.5
1/12+10s	1/14+12s	21:41	5.9	2.4
1/14+12s	multi-bunches	18:25	4.0	4.3

multi-bunches: 12 units composed of 160 sequential buckets filled with some 50-μA current each followed by 43 empty buckets were equally spaced around the storage ring.

203 bunches: equally spaced 203 buckets, i.e., every 12 buckets, were filled with 0.5-mA current each.

1/12+10s: Consecutive 203 buckets were filled with electrons; 203 buckets corresponds to 1/12 of the total bucket number of 2436 of the storage ring. The remaining 11/12 part of the ring is filled with equally spaced 10 isolated bunches with 1.5-mA current each, i.e., every 203 buckets were filled with 1.5-mA current. The current of 1/12 part was 85 mA.

1/14+12s: Consecutive 174 buckets were filled with electrons; 174 buckets correspond to 1/14 of the total bucket number of the storage ring. The remaining 13/14 part of the ring is filled with equally spaced 12 isolated bunches with 1.6-mA current each, i.e., every 174 buckets were filled with 1.6-mA current. The current of 1/14 part was 80 mA.

Table 2. RMS values of differences between two different times of the measurement within the same filling pattern: $RMS_{x/y}(FP1_1\text{-}FP1_2)$

filling pattern 1	filling pattern 2	Δt (min. : sec.)	RMS_x (mm)	RMS_y (mm)
multi-bunches	multi-bunches	12:14	5.1	2.8
203 bunches	203 bunches	21:30	6.4	1.9
1/12+10s	1/12+10s	20:21	6.6	2.3
1/14+12s	1/14+12s	18:48	3.3	2.3

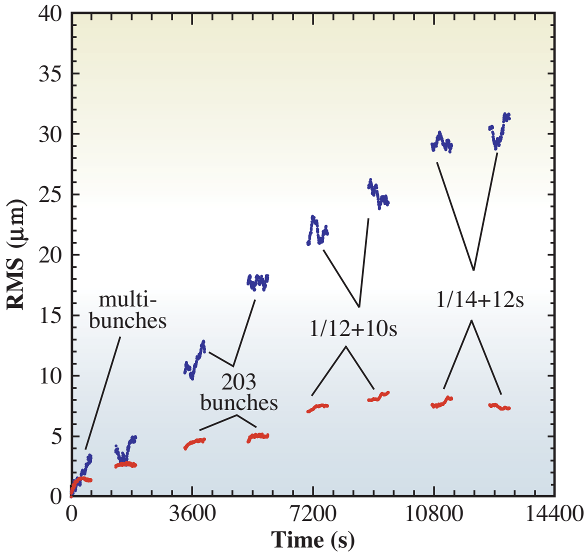

Fig. 7. RMS values of the difference between the measured position data from the measurement at the reference time. Horizontal axis: time in seconds from the starting time: $\Delta t = t\text{-}t_0$. Vertical axis: RMS values in μm: $RMS_{x/y}(t\text{-}t_0)$. Blue marks are in horizontal direction ($RMS_x(t\text{-}t_0)$). Red marks are in vertical direction ($RMS_y(t\text{-}t_0)$). The filling patterns are indicated in the plot. Explanations of each filling pattern are described in the caption of Table 1. Each filling pattern was repeated twice. The blank regions between the data points were the time for discard and refill of the beam, in which the COD measurements could not be carried out.

Development of Bunch-by-Bunch Feedback

Currently, a high-current bunch of more than 10 mA/bunch can be stored in the storage ring by suppressing the horizontal and vertical mode-coupling single-bunch instabilities with the bunch-by-bunch feedback system (BBF). However, the high gain or short feedback damping time of less than 1 ms of the BBF is necessary to suppress these instabilities. Simultaneously, a wide horizontal acceptance of the BBF is required to suppress the horizontal betatron motion excited by the formation of the injection bump orbit. To meet those requests, we increased the feedback strength by introducing of high-power amplifiers, and we are constructing a high-efficiency horizontal kicker (Fig. 8). For the longitudinal feedback for possible low-energy high-current operation in the near future, the new type of longitudinal kicker with high shut impedance per unit length is also under construction.

Moreover, we are developing a tune-tracking RFKO system for the booster synchrotron based on the bunch-by-bunch feedback system. Currently, the booster is operating every seconds during the wait of the injection to stabilize the system. However, the on-demand operation of the booster is preferred for saving of electricity. With this mode, betatron tune drift occurs in this operation mode because of the unstable temperature of the magnet system and it is difficult to perform the bunch purification by RFKO. To overcome this tune drift, we are testing the tune tracking RFKO system shown in Fig. 9. The main bunch is excited by the bunch-by-bunch feedback system and the oscillation signal is sent also to the RFKO system. The bunch-by-bunch feedback system uses an FIR filter less than ten taps and the tracking speed to the tune is fast enough. The tune shift between the main bunch and satellite bunches produced by the current dependent tune shift is also intended to be compensated by the BBF by careful adjustment of the phase of the FIR filters. In a preliminary test, we obtained the purity of 10^{-8} to 10^{-9}, which is not sufficient for the required purity of 10^{-10}; further development is necessary.

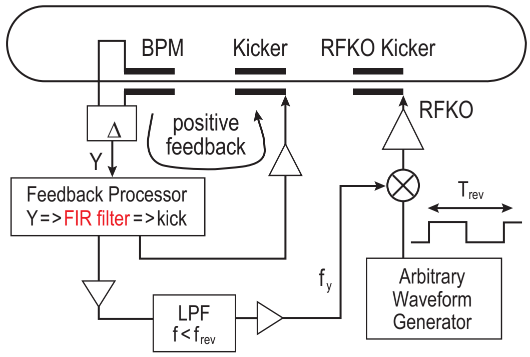

Fig. 9. Tune tracking RFKO system. The vertical betatron motion of the main bunch is excited by the feedback processor (positive feedback loop). The oscillation signal is also fed to the RFKO system to kick out the satellite bunches. The negative vertical tune shift of the main bunch is intended to be compensated by the feedback.

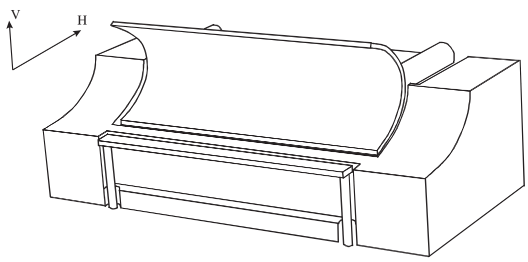

Fig. 8. High-efficiency horizontal kicker. One quadrant is shown with a large horizontal electrode of full shape. The vertical kicker electrode is also shown in the bottom of the figure.

Beam Loss Monitor

One of the major concerns in the SPring-8 storage ring (SR) is irradiation-induced damage due to beam loss to the environment surrounding the accelerator. In 2003, a vacuum leakage was caused by the meltdown of a vacuum chamber at the injection section during the time of a beam abort [4]. In addition, demagnetization of permanent magnets for the in-vacuum insertion devices (IDs) is caused by the irradiation of circulating electron beam in the SR [5].

To observe a beam loss, to manifest its mechanism, and to handle it, a beam loss monitoring system has been developed. The beam loss monitor is composed of a beam loss detector and a noise detector. The former detects secondary particles with PIN photodiodes, of which the spectral range of the sensitivity is 780 ~ 1100 nm, the radiant sensitive area is 2.65×2.65 mm^2 and no reversed bias voltage is given, when a circulating electron beam hits a vacuum chamber and is lost. The latter is used to compensate for background noises (see Fig. 10). Each detector is shielded by an aluminum chassis of $50 \times 80 \times 34$ mm^3 and is set to characteristic points in the tunnel of the SR such as the injection point, the beam dump point, the chamber for the irradiation experiment (SS48), and the entrance of the long in-vacuum ID (ID19). These signals are extracted through a shielded two-pair twist cable into a signal processing circuit outside the tunnel, and then digitized using a digital recorder (GR-7500). The signal is monitored in the central control room.

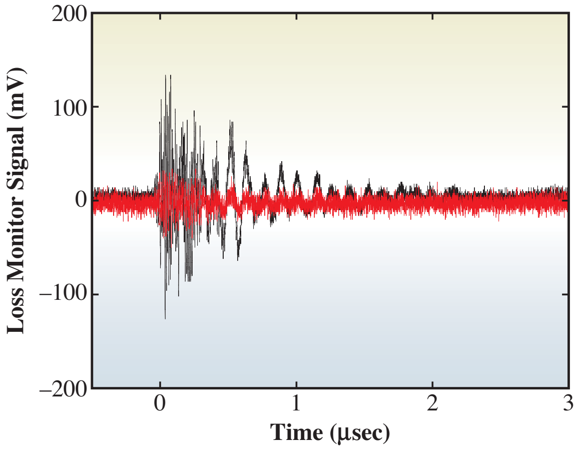

Fig. 10. Background noise detected using a beam loss monitor before (black) and after (red) compensation, when the injection bump magnet is turned on.

By monitoring beam losses with beam loss monitors set around the SR, it can be specified where the beam loss occurs. A typical beam loss signal on the nominal injection is shown in Fig. 11. The beam loss signal was observed at the injection point and at the SS48. An injected beam coherently oscillates around the reference orbit because of the off-axis injection scheme. From Fig. 11, we see that a part of the injected beam hits the vacuum chamber and is lost at the injection point and at the SS48. In this case, one can expect that, by locally deforming the reference orbit around there, this part can survive and achieve an equilibrium beam distribution, and the injection efficiency from the injector to the SR will improve. An example of such experiments is shown in Fig. 12, where the bump orbit was locally set in the vertical direction at the SS48. The average injection efficiency became higher as the height of the local bump was increased. This indicates that the irradiation damage due to beam loss surrounding the SR on the timing of nominal injection can be more or less suppressed.

In the future, we will strategically install additional beam loss monitors to watch and handle beam losses effectively.

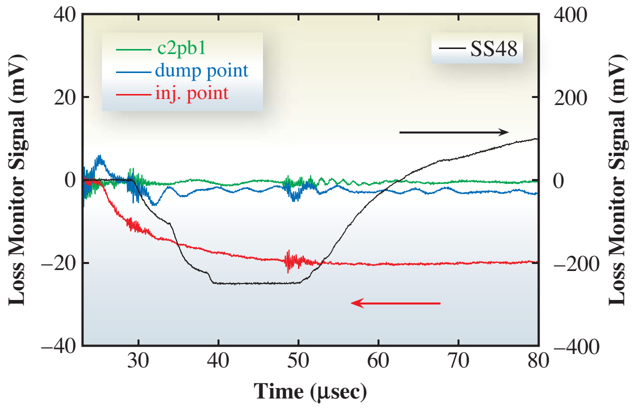

Fig. 11. Beam loss signal measured using a beam loss monitor on nominal injection. "c2pb1" denotes beam loss monitor set near absorber-3 of cell-2 in SR.

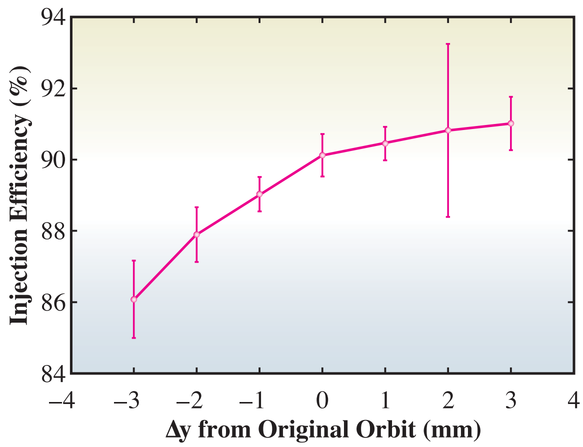

Fig. 12. Injection efficiency (SR/SSBT) dependent on vertical local bump orbit at SS48.

Development of Accelerator Diagnostics Beamlines

The generation of short X-ray pulses is now a challenge at SPring-8. The visible streak camera at the accelerator diagnostics beamline I (BL38B2) provides crucial information on the longitudinal bunch structures of the electron beam essential to tackle the challenge. One approach to generate shorter synchrotron radiation pulses is to shorten the bunch length itself by decreasing the momentum compaction factor α of the storage ring. The natural bunch length is proportional to the square root of factor α. The longitudinal bunch profiles measured using the streak camera confirmed that the bunch length was successfully shortened to about one-third by decreasing α by one order (Fig. 13). Another approach to obtain short X-ray pulses is by slitting a vertically tilted bunch. By giving a pulsed vertical kick to an electron bunch, the head-tail oscillation of the bunch can be excited in the presence of nonzero vertical chromaticity. Figure 14 shows the vertical beam tilt observed using the streak camera operated in the dual-time scan mode. The maximum observed difference between the head and tail of the bunch was about 2 mm. Further studies to obtain short X-ray pulses by this method are in progress.

The accelerator diagnosis beamline II (BL05SS) has an ID light source and two optics hutches. In April 2008, we successfully delivered the first ID light to the optics hutch II that contains a cryogenically cooled monochromator. We are now investigating the diagnostics of both the transversal and longitudinal properties of the electron beam by observing the imprints on the spectral, spatial, and temporal characteristics of the synchrotron radiation of the ID. The magnet array mounted on the ID is of Halbach type with 51 periods 76 mm long. The maximum value of the deflection parameter K is 5.8 when the magnet gap is minimum at 20 mm. The spectral photon fluxes of the ID were measured for both the regular user optics (ε=3.4 nm·rad) and the low-α optics mentioned above (ε=24.8 nm·rad). Figure 15 and Fig. 16 show spectral fluxes of the 1st and 19th harmonics, respectively. The peak of higher harmonics as high as 19 is clearly observed, which shows success of the elaborate tuning of the magnetic field in the assembling of the ID. The observed spectra of the low-α optics show reduction of the peak intensity and growth of the tail in the low-energy region, which are distinct imprints of large emittance of the electron beam.

We have been developing a method for the real-time measurement of the energy spread of the electron beam on the basis of idea of observing the divergence of monochromatic higher harmonics of the ID in the vertical direction. The vertical divergence is sensitive to the energy spread of the electron beam because of the small vertical emittance of SPring-8, while the horizontal divergence is dominated by the horizontal emittance. To demonstrate our idea, we observed the vertical profile of the 19th harmonics of the ID while changing the effective beam energy spread. The effective energy spread was increased by exciting the beam energy oscillation by modulating the phase of the RF voltage at the synchrotron

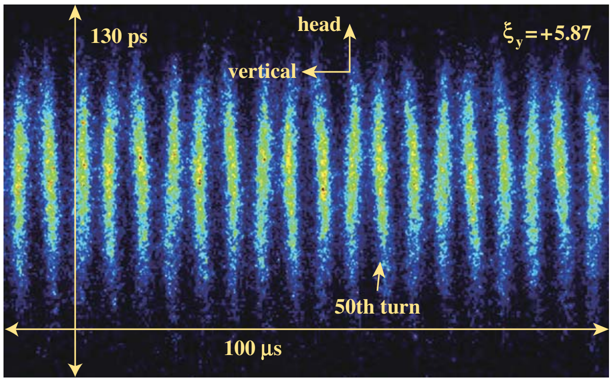

Fig. 14. Excited head-tail oscillation of a stored electron bunch observed using the visible streak camera operated in the dual time scan mode.

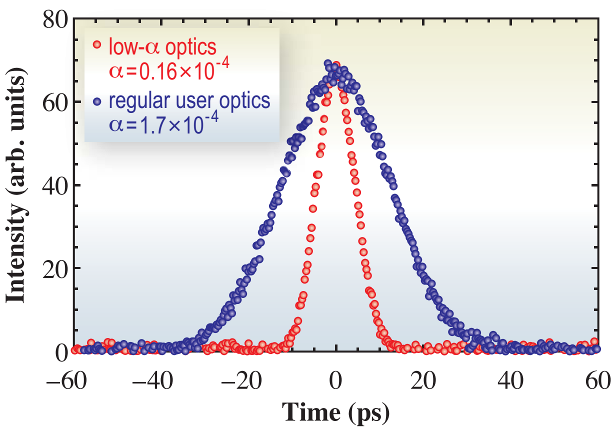

Fig. 13. Longitudinal bunch profiles measured for low-α and regular user optics, respectively. The bunch length was successfully made shorter by decreasing α.

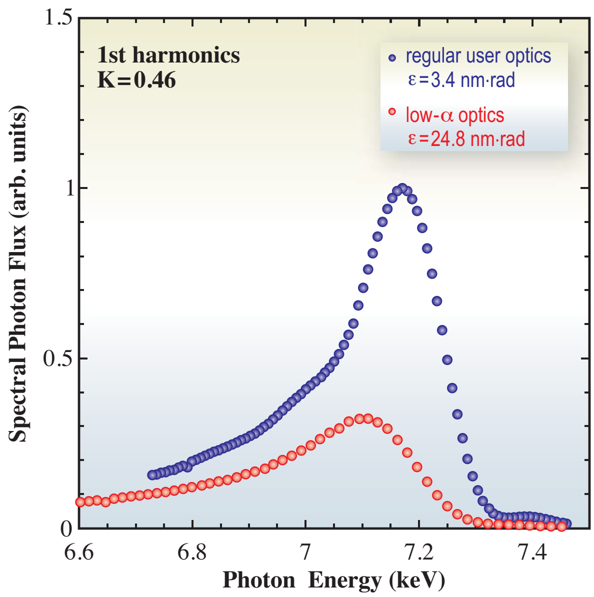

Fig. 15. Spectral photon fluxes of the 1st harmonics of the ID. The magnet gap was 80 mm and the deflection parameter K was 0.46. The blue and red dots show the spectra measured for the regular user and the low-α optics, respectively.

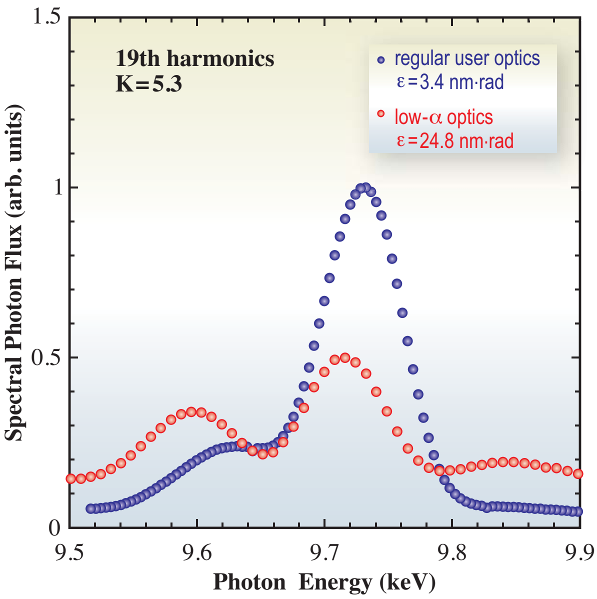

Fig. 16. Spectral photon fluxes of the 19th harmonics of the ID. The magnet gap was 22 mm and the deflection parameter K was 5.3. The blue and red dots show the spectra measured for the regular user and the low-α optics, respectively.

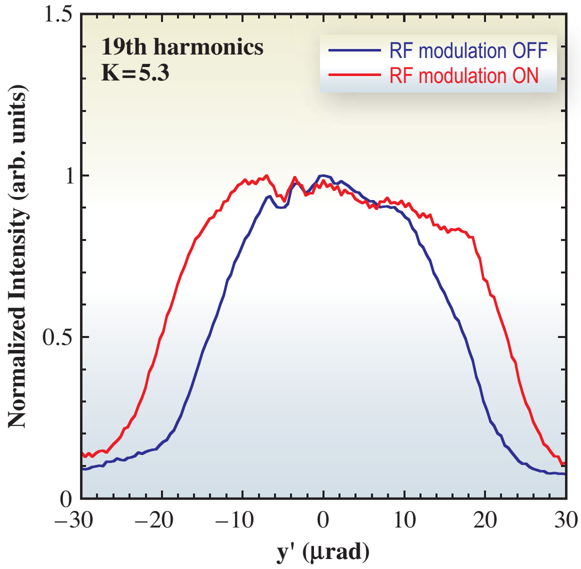

Fig. 17. Measured vertical profiles of the 19th harmonics of the ID with and without the phase modulation of the RF voltage. The magnet gap was 22 mm. The red line shows the data with RF phase modulation of 4 degrees corresponding to the effective beam energy spread of 0.27%. The blue line shows the data without the modulation when the beam energy spread is 0.11%.

frequency (f_s~ 2 kHz). An X-ray CCD camera was used and the exposure time was set at 30 ms, which is sufficiently longer than the period of the energy oscillation. Preliminary results are shown in Fig. 17. Although preliminary, the results are promising and encourage us to develop, by employing a fast-gated camera, turn-by-turn diagnostics of the energy spread of a nonequilibrium beam such as an injection beam that is expected in the future from the C-band XFEL driver.

To observe the temporal structure of X-ray pulses from the ID, we are investigating the characteristics of an X-ray streak camera such as dependence of the temporal resolution on the photon energy. With the aim of developing optical diagnostics for expected next-generation light sources, we are preparing to observe shorter X-ray pulses generated by low-α operation of the ring and by slitting vertically tilted bunch obtained by exciting head-tail motion.

At the diagnosis beamline II, the so-called edge radiation from the bending magnets upstream and downstream of the ID straight section can be observed. Formerly, a movable mirror to direct FIR laser beam to the electron beam traversing the straight section was installed downstream of the lower bending magnet for a plan in progress to generate Compton-backscattered MeV γ-ray photons. By applying the mirror to direct the edge radiation into the atmosphere, we observed the edge radiation with microwave detectors. The intensities in the 50-75 GHz and 75-110 GHz frequency bands were measured by increasing the current of a single-bunch beam. The measured turn-by-turn intensities in the two bands varied temporally and the time-averaged intensities showed nonlinear dependence on the bunch current (Fig. 18), which suggested that we detected coherent synchrotron radiation originating from single bunch instabilities.

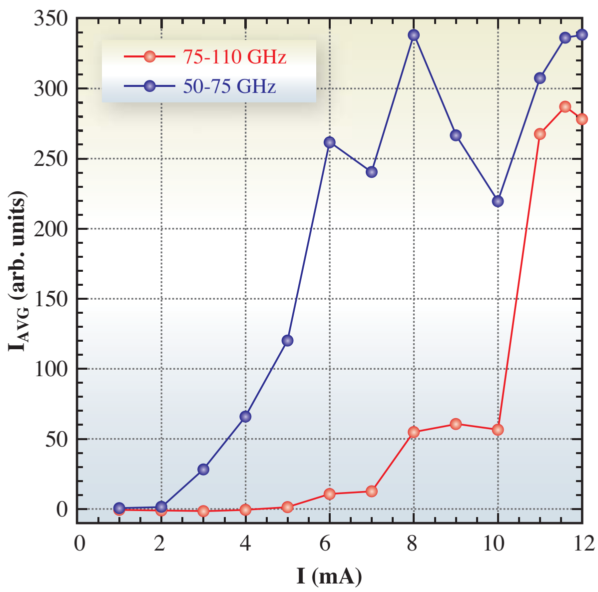

Fig. 18. Time-averaged intensities of the edge radiation measured in the 50 - 75 GHz and 75 - 110 GHz microwave bands as functions of the current of single-bunch beam.

Investigation of Misreading of Pressure Measurement by Radiation

The vacuum pressures of the SPring-8 storage ring became better, with the increase in the integrated beam dose until the summer shutdown of August 1997. However, after the summer shutdown, the pressure readings of the Bayard-Alpert vacuum gauge (ionization gauge) around the photon absorbers did not decrease.

Assuming that the pressure readings of the ionization gauges are affected by the synchrotron radiations scattered by the photon absorbers, radiation shields were added around the gauge heads and cables. In addition to the shields, U-shape pipe or a permanent magnet was installed in 2001 between the gauge duct and the beam duct of the storage ring to eliminate the photoelectrons. As a result of the countermeasures, the pressure at the Absorbers (AB3) and the Crotch Absorbers (CR1) became equivalent to the pressure at the Straight Section Chambers (SC1), as shown in Fig. 19. Figure 19 shows the pressure rise normalized by the beam current and the product of the beam current and the beam lifetime as a function of the integrated beam dose.

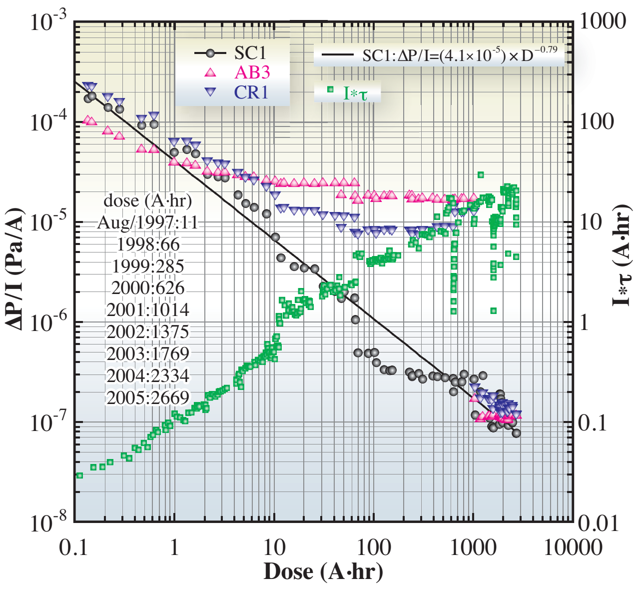

Fig. 19. Pressure rise normalized by beam current ($\Delta P/I$) and the product of the beam current and beam lifetime ($I \cdot \tau$). The beam lifetime was measured when the gaps of all Insertion Devices were fully opened in the beam filling of multi-bunch mode. The pressures at Straight Section Chambers (SC1) that are far from the photon absorber decreased with increasing integrated beam dose. However, the pressures at Absorbers (AB3) and Crotch Absorbers (CR1) did not decrease after 10 A·hr of beam dose.

Some effects of irradiation to the gauge cable and a large amount of electronic inflow to the gauge head are expected. However, very little is known about the effect of irradiation to the gauge head. To investigate the mechanism for misreading of the vacuum pressure, we conducted the irradiation experiment of the vacuum gauge at the accelerator diagnosis beamline II (BL05SS), as shown in Fig. 20. The experimental result of the collector currents against the pressure is shown in Fig. 21. When the collector electrode is irradiated at the pressure of less than 0.1 Pa, the collector currents indicate a constant value of 2×10^{-11} A. Because the collector currents are expected to be caused by the photoelectric emission of the photoelectric effect or the Compton scattering, the collector currents are constant against the pressure change.

Meanwhile, when the collector electrode is not irradiated, the photoelectric emission is not generated and the collector currents decrease with pressure. The ion currents of the collector electrode are generated by the residual gases ionization by X-ray, so the collector currents correlate with the pressure.

A part **[A]** of Fig. 21 is considered to be the residual gases ionization. However, the cause of part **[B]** is the residual gas ionization or another process is not confirmed.

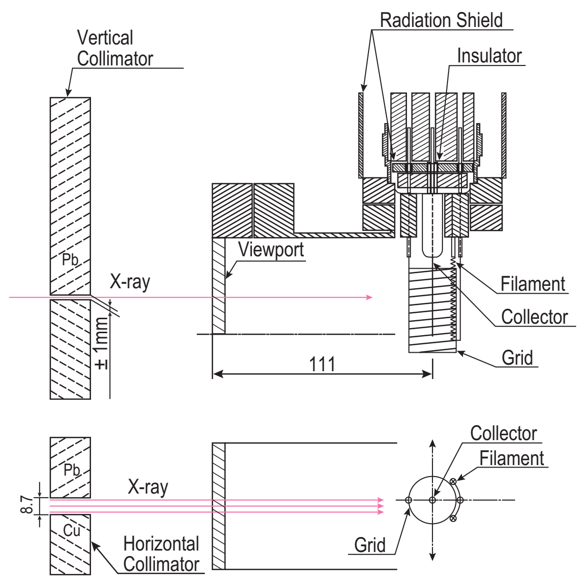

Fig. 20. Experimental setup at the front-end of the Accelerator Diagnosis Beamline II (BL05SS). The gauge head is installed in the vacuum chamber with the view port. The chamber is set on XZ precision motorized stages, so as to move the collector electrode. The collector current of irradiated gauge head is measured under various pressures.

The photoelectric emission by the photoelectric effect or by the Compton scattering is deduced to be dominant factor for the misreading of the vacuum pressure, and the ionization of residual gases is almost negligibly small under 1×10^{-4} Pa. However, between the gauge head and the electric connector, there is atmospheric air. If the X-rays irradiate the atmospheric air gases between the gauge head and electric connector, the gases are ionized and a large amount of collector currents are generated. It is known empirically as a necessity of the radiation shield for the electric connector; this indicates that the cause of misreading is the ionization of atmospheric air between the gauge head and electric connector.

In this investigation, the causes of the misreading of the Bayard-Alpert vacuum gauge (ionization gauge) by irradiation were confirmed. It is necessary to further investigate about the atmospheric air ionization process between the gauge head and electric connector, and the photoelectric emission mechanism of the photoelectric effect or the Compton scattering from the collector electrode.

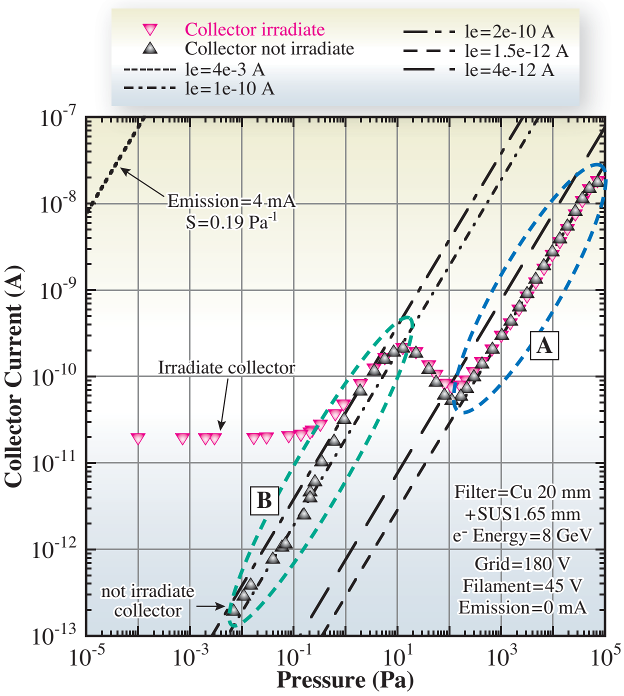

Fig. 21. An experimental result of the measured collector currents against the pressure. The emission current of the gauge is shut off, so the collector current cannot flow under normal circumstances. The symbol ▽ indicates the collector currents with the irradiation and the symbol ▲ without the irradiation.

Research and Development of Femtosecond Pulse X-Ray Generation

The generation of an X-ray with an energy of 10.7 keV and a pulse width of 600 fs in two standard deviations can be achieved if we install superconducting crab cavities and a minipole undulator in one of the long straight sections of the SPring-8 storage ring. The flashing repetition of such an X-ray is the same as that of the preexisting synchrotron radiation, or that of the electron bunches circulating around the ring. This feature complements the low repetition of the X-FEL, which has extraordinarily high temporal intensities. This method, in addition, can supply a femtosecond X-ray without causing any disturbance to users on the other beam lines at SPring-8. Its principle of generation, performance expected with design parameters, and R&D issues have been described in previous reports [6,7].

Because the stability of the electron orbit in the storage ring is insensitive to the common phase shift among deflecting cavities, the RF power from a 1 MW klystron, a power amplifier, is quartered and supplied to four crab cavities. Each is fed into the cavity through a fast high-power phase shifter newly developed for precise deflecting phase control (Fig. 22). The achieved performance of this phase shifter through high-power tests was as follows: the phase-adjusting range was ±1.5 degrees under a full reflection power of 300 kW and the frequency response of the phase change was from DC to 1 kHz (–3 dB). This response speed is sufficient to suppress the individual phase fluctuation of crab cavities, which is caused mainly by their change in resonant frequency. The test results of a crab cavity at KEK show that the resonant frequency of the cavity is

Fig. 22. 300 kW fast phase shifter in the magnetic shield (blue). Incident power travels from right to left and is reflected with a variable-position short plate found under the ladder bridge.